

Accepted Manuscript

Numerical simulation of the nonlinear ultrasonic pressure wave propagation in a cavitating bubbly liquid inside a sonochemical reactor

Hakan Dogan, Viktor Popov

PII: S1350-4177(15)30077-8

DOI: <http://dx.doi.org/10.1016/j.ultsonch.2015.11.011>

Reference: ULTSON 3039

To appear in: *Ultrasonics Sonochemistry*

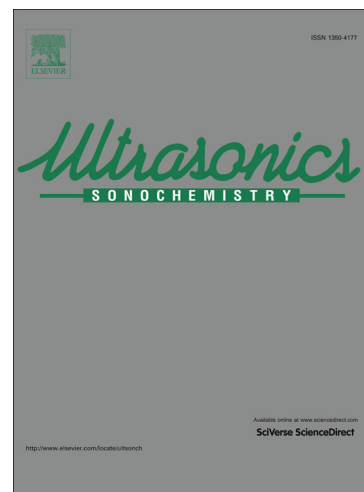
Received Date: 18 June 2015

Revised Date: 28 October 2015

Accepted Date: 12 November 2015

Please cite this article as: H. Dogan, V. Popov, Numerical simulation of the nonlinear ultrasonic pressure wave propagation in a cavitating bubbly liquid inside a sonochemical reactor, *Ultrasonics Sonochemistry* (2015), doi: <http://dx.doi.org/10.1016/j.ultsonch.2015.11.011>

This is a PDF file of an unedited manuscript that has been accepted for publication. As a service to our customers we are providing this early version of the manuscript. The manuscript will undergo copyediting, typesetting, and review of the resulting proof before it is published in its final form. Please note that during the production process errors may be discovered which could affect the content, and all legal disclaimers that apply to the journal pertain.



Numerical simulation of the nonlinear ultrasonic pressure wave propagation in a cavitating bubbly liquid inside a sonochemical reactor

Hakan Dogan¹ & Viktor Popov²

¹Institute of Sound and Vibration Research, University of Southampton, Southampton, UK

²Ascend Technologies Ltd, Eastleigh, UK

Abstract

We investigate the acoustic wave propagation in bubbly liquid inside a pilot sonochemical reactor which aims to produce antibacterial medical textile fabrics by coating the textile with ZnO or CuO nanoparticles. Computational models on acoustic propagation are developed in order to aid the design procedures. The acoustic pressure wave propagation in the sonoreactor is simulated by solving the Helmholtz equation using a meshless numerical method. The paper implements both the state-of-the-art linear model and a nonlinear wave propagation model recently introduced by Louisnard (2012), and presents a novel iterative solution procedure for the nonlinear propagation model which can be implemented using any numerical method and/or programming tool. Comparative results regarding both the linear and the nonlinear wave propagation are shown. Effects of bubble size distribution and bubble volume fraction on the acoustic wave propagation are discussed in detail. The simulations demonstrate that the nonlinear model successfully captures the realistic spatial distribution of the cavitation zones and the associated acoustic pressure amplitudes.

Keywords: nonlinear propagation, acoustic cavitation, bubble dynamics

Contact details: H. Dogan (email: dgnhkn@gmail.com), V. Popov (email: viktor@ascendtechnologies.co.uk, popov_v@yahoo.com)

List of Figures

Figure 1: Thermal, viscous and acoustic dissipation for a $R_0 = 5\mu\text{m}$ bubble in water. The thick solid line is the non-dimensional viscous dissipation; whereas thick dashed line represents the non-dimensional thermal dissipation and the dash-dot line the non-dimensional acoustic dissipation. Note that the non-dimensionalization is done with respect to $p_0 V_0 \omega$, i.e. $\Pi_v^* = \Pi_v / p_0 V_0 \omega$. The thin vertical dashed line represents the Blake threshold.

Figure 2: Thermal, viscous and acoustic dissipation for a $R_0 = 10\mu\text{m}$ bubble in water. The line types are identical to the ones in Fig. 1.

Figure 3: The real and imaginary part of the wavenumber used in the nonlinear wave propagation, evaluated by using Π_{th} , Π_{rad} and Π_v with $R_0 = 5\mu\text{m}$ and $\beta = 0.005\%$. Eqs. (12-13) are used to compute the values. Note that $\text{Re}(k^2)$ and $\text{Im}(k^2)$ should be first cast into a complex number, then square root of k^2 leads to the results presented in this figure.

Figure 4: A sketch for the source nodes and local sub-domains placed in the solution domain Ω , and on the global boundary Γ .

Figure 5: The ramp function used for updating the real and imaginary parts of the wavenumber from their initial value to their final profile given in Figure 3. The supplementary file Video 1 shows how the wavenumber profile changes as the increments to the bubble void fraction are applied (see [web-link-1](#)).

Figure 6: Pressure profiles with increasing bubble volume fraction, β . $U_0 = 5\mu\text{m}$ and $R_0 = 5\mu\text{m}$.

Figure 7: Pressure profiles for the cases: $U_0 = 0.2\mu\text{m}$, $U_0 = 0.5\mu\text{m}$ and $U_0 = 5\mu\text{m}$. The attached Video 2 shows the convergence of the solution for the case $U_0 = 5\mu\text{m}$, together with the text files which report the RMS error statistics (see [web-link-1](#)).

Figure 8: Comparison of wave profiles for a displacement amplitude of the acoustic source of $5\mu\text{m}$. The thick line shows the nonlinear propagation, the dashed curve corresponds to the linear result and the thin line represents the pure liquid case.

Figure 9: A sketch of the sonoreactor designed by CEDRAT Technologies. (a) perspective view (T – transducer, H – heater) and (b) x - y plane.

Figure 10: Effect of bubble volume fraction on the linear wave propagation ($R=10$ - $100\mu\text{m}$).

Figure 11: Pressure wave distribution obtained from the nonlinear model at (a) $s/N_s = 0.005$, (b) $s/N_s = 0.01$ and (c) $s/N_s = 1$ (final result) vs. (d) the linear model.

ACCEPTED MANUSCRIPT

1. Introduction

The use of ultrasound is beneficial in many engineering applications such as cleaning of medical devices [1], treatment of waste water [2], textile cleaning [3], and fragmentation of ureteric and kidney stones [4]. As reviewed by Gogate [5] and Mason [6], the applications can vary from microscale setups for crystallization, polymer chemistry (for initiation of reactions or for destruction of complex polymer structures) and intercellular protein recovery to industrial operations such as refining of fossil fuels, extraction of coal tars, air cleaning as well as removal of biological/chemical contamination. Important guidelines for process intensification, reactor design, and recommendations for further research and development can be found in references [5, 7].

A high intensity acoustic source may achieve high level pressure amplitudes in the medium which, over a certain pressure threshold, initiate the cavitation phenomenon, the bubble clouds and the streamers. The sonochemical reaction gains its efficiency from the cavitation and the ultrasonic energy stored in bubble oscillations. When close to a solid surface, e.g. textile, many microbubbles collapse creating a jet with very high velocity towards the solid surface [8]. The jets can push the nanoparticles and lodge them into the surface, in this case textile, with such force that they would stay on the surface even after a number of washing cycles.

Some processes are easier to be scaled-up when designing a reactor, e.g., the mixing, species transport and heat transfer. All three processes can be analysed by employing the computational fluid dynamics. Processes which cannot be easily analysed are the estimation of the cavitation zone and the acoustic pressure distribution in the reactor. The major obstacle during the design is that the whole process is highly non-linear as there are several parameters that are not known in advance, e.g., location and geometry of the cavitation zone, bubble fraction, acoustic pressure distribution [9]. The fact that there is no software package available which could solve this problem makes this issue even more significant.

Despite the extensive research at laboratory scale, a limited number of sonochemical reactors have been built on a full-scale for industrial applications, mainly due to [10, 11]: (i) the lack of straightforward theory to determine the location and the cavitation collapse rate as a function of operating and reactor design properties, (ii) the very high degree of uncertainty when

scaling up the existing information on sonochemical processes in laboratory conditions, (iii) large range of spatial and temporal scales involved in ultrasonic cavitation and (iv) the existence of cavitation near the transducer's surface which causes energy dissipation patterns in the reactor which are difficult to predict.

In this article, acoustic wave propagation inside a sonochemical reactor, which employs ultrasound energy for impregnation of textile materials with antibacterial nanoparticles, is investigated. The pressure field inside the reactor is simulated as it can be used to predict the regions of high energy bubble clouds, and to optimize the geometry and mode of operations of sonochemical reactors [12]. The obtained distribution of the cavitation zones closely relates to the coating of the textile as the corresponding jet and collapse events significantly contribute to the nanoparticles' impregnation process (e.g. ZnO and MgO) [13, 14, 15, 16]. The designed sonoreactor consists of three cylindrical transducers, each emitting pressure waves at 20 kHz. The reactor is filled with liquid that may be ethanol, water or a mixture of the two.

Recently, Louisnard [17] has published a wave propagation model, recasting the time domain Caflisch equations [18] into a nonlinear Helmholtz equation using an elegant mathematical approach. In addition, a conservation of energy formula is given for the bubbly medium which allows an explicit definition of dissipation mechanisms upon performing cycle averaging. The latter point is highly important when defining more precisely the effects of bubble motion on the attenuation of waves which is underestimated by the linear theory.

Numerical simulations which use nonlinear propagation theories are rather scarce in the literature. Louisnard used COMSOL Multiphysics software in order to present results on the nonlinear dissipation and self-attenuation of waves [17] and the formation of streamers [19]. Simulations of Vanhille and Campus-Pozuelo [20, 21] are essentially nonlinear because they solve for the full form of the time-dependent Caflisch equations by coupling with the time-dependent volumetric oscillations of the bubble field which successfully simulates the self-attenuation sound pressure and generation of higher harmonics. The volumetric pulsations of bubbles is formulated with a damped-oscillator equation; though this may be violated when the driving pressure amplitude is high as the bubbles experience 1-2 orders of magnitude increment in their volumes. Servant and co-workers [22, 23, 24] performed computational fluid dynamics

simulations solving for the coupled Caflisch equations [18]. They were able to predict the pressure distribution and verify their results by comparison with the erosion of an aluminium foil by cavitation bubbles [23], though this comparison indicated qualitative agreement rather than quantitative. Some iterative solutions accounting for inhomogeneous bubble population field have also been performed in [25, 26, 27], however the main equation solved was essentially the linear method proposed in [28].

Tudela et al. [29] reviewed the numerical methods which simulate the spatial distribution of the acoustic pressure waves in sonochemical reactors and assessed the existing approaches in terms of their qualitative and quantitative results in comparison to experiments. Perhaps, their concluding remarks on new challenges and trends in coming years best indicate the importance of the present study: “Development of a more rigorous acoustics model accounting for the nonlinear propagation of sound waves and the attenuation of the sound pressure by cavitation is also necessary”. The present work just undertakes that development task which potentially fills a gap in the simulation stage by demonstrating a solution procedure for the nonlinear Helmholtz equation proposed in [17].

2. Theory

The equation of conservation of mass and momentum for a mixture containing bubbles and liquid are given by [18]

$$\frac{1}{\rho c^2} \frac{\partial p}{\partial t} + \nabla \cdot \vec{v} = \frac{\partial \beta}{\partial t} \quad (1)$$

$$\rho \left(\frac{\partial \vec{v}}{\partial t} + (\vec{v} \cdot \nabla) \vec{v} \right) + \nabla p = 0 \quad (2)$$

where $p(\vec{r}, t)$, $\vec{v}(\vec{r}, t)$ and $\beta(\vec{r}, t)$ are the spatio-temporal acoustic pressure field, velocity field and void fraction of bubbles, respectively, ρ is the density of the liquid and c is the sound speed

in the host medium. For a mono-disperse bubble distribution, the bubble volume fraction is defined as

$$\beta = \frac{4}{3}\pi R^3 N \quad (3)$$

where N is the number of bubbles per unit volume and R is bubble radius.

The radial dynamics of bubbles, accounting for the liquid compressibility to first order, is modelled by the well-known Keller-Miksis equation

$$\left(1 - \frac{\dot{R}}{c}\right) R \ddot{R} + \frac{3}{2} \left(1 - \frac{\dot{R}}{3c}\right) \dot{R}^2 = \frac{1}{\rho} \left(1 + \frac{\dot{R}}{c} + \frac{R}{c} \frac{d}{dt}\right) \left(p_g - \frac{2\sigma}{R} - \frac{4\mu\dot{R}}{R} - p\right) \quad (4)$$

where σ is surface tension, μ is the viscosity of the liquid and the overdots denote the total differentiation with respect to time. The pressure p in the liquid host medium is hypothetically assumed at the location of the bubble if the bubble were absent and is defined as

$$p = p_0 - P \sin \omega t.$$

During the growth and the compression of a bubble undergoing stable cavitation, the internal gas pressure p_g and the temperature may be subject to rapid changes. Heat transfer between the gas phase and the liquid during the oscillations causes overall thermal energy losses in the medium. The application of the ideal gas (polytropic) law, which assumes the spatial uniformity of the pressure and the temperature fields within the bubble, may well underestimate the net thermal losses. Therefore, we incorporate the nonlinear model based on solving the continuity and the energy conservation equations for a gas (as in Ref. [30]) into the formulation.

The state-of-the-art linear model for modelling pressure waves in bubbly liquids is the formulation proposed by Commander and Prosperetti [28]. In that model, it is assumed that the

bubble radius exhibits small variations, i.e. $R = R_0(1 + x)$ with $x \ll 1$. Accordingly, the acoustic, viscous and thermal losses are accounted for with linearized expressions. Assuming harmonic oscillations of all fields, the wave equation of the linear model in the frequency domain is expressed as

$$(\nabla^2 + k_{\text{lin}}^2) p = 0 \quad (5)$$

where the wavenumber k_{lin} in the bubbly liquid is given by the relation

$$k_{\text{lin}}^2 = \frac{\omega^2}{c^2} + 4\pi\omega^2 \int_0^\infty \frac{R_0 N(R_0)}{\omega_0^2 - \omega^2 + 2ib_{\text{tot}}\omega} dR_0, \quad (6)$$

with $N(R_0)dR_0$ being the number of bubbles per unit volume with radii between R_0 and $R_0 + dR_0$. The explicit expressions for the damping coefficient b_{tot} and the bubble resonance frequency ω_0 can be found in [28, 30].

The nonlinear wave propagation is based on the representation of a global energy conservation and mechanical energy balance of the entire two-phase medium such that the energy dissipated by bubbles and thus the total reduction in acoustic energy delivered to the medium is fully quantified. Considering a driving sound field with acoustic period $T = 2\pi/\omega$, the mechanical energy conservation is given as [31]:

$$\nabla \cdot \langle p \vec{v} \rangle = -N(\Pi_{th} + \Pi_v + \Pi_{rad}). \quad (7)$$

The right hand side (RHS) terms in (7) are described as period-averaged thermal, viscous and acoustic dissipation functions [17, 31], respectively, which can be significantly different compared to their linear counterparts especially above the cavitation threshold, and are defined as follows:

$$\Pi_{th} = \frac{1}{T} \int_0^T - \left(p_g + \frac{\dot{R}}{c} p_g + \frac{R}{c} \dot{p}_g \right) \frac{\partial V}{\partial t} dt, \quad (8)$$

$$\Pi_v = \frac{1}{T} \int_0^T 16\pi\mu \left(R\dot{R}^2 + \frac{R^2\dot{R}\ddot{R}}{c} \right) dt, \quad (9)$$

$$\Pi_{rad} = \frac{4\pi}{Tc} \int_0^T R^2\dot{R} \left(\dot{R}p + \dot{p}R - \frac{1}{2}\rho\dot{R}^3 - R\dot{R}\ddot{R} \right) dt, \quad (10)$$

Eq. (7) shows that the acoustic energy delivered to the bubbly liquid is dissipated by the bubble population field by the viscous, thermal and radiation losses during the radial oscillations.

In the following, the nonlinear dissipation functions are plotted. Figure 1 displays the thermal, viscous and acoustic dissipation from a bubble with radius $R_0 = 5 \mu\text{m}$ in water. Following values for the material properties in the ambient liquid are used: $\rho = 1000 \text{ kg/m}^3$, $\mu = 0.001003 \text{ kg/ms}$, $\sigma = 0.0725 \text{ N/m}$ and the sound velocity $c = 1500 \text{ m/s}$. The hydrostatic pressure is taken as $p_0 = 101300 \text{ Pa}$. The dashed-dotted thin vertical line in the figure refers to the Blake threshold which is given by the relation $p_B = p_0 + \frac{8\sigma}{9} \sqrt{\frac{3\sigma}{2R_0^3(p_0 + 2\sigma/R_0)}}$. The thermal and the viscous dissipation dominate for very low amplitude driving, acoustic dissipation effects are much higher than the others for larger amplitude driving especially over the Blake threshold.

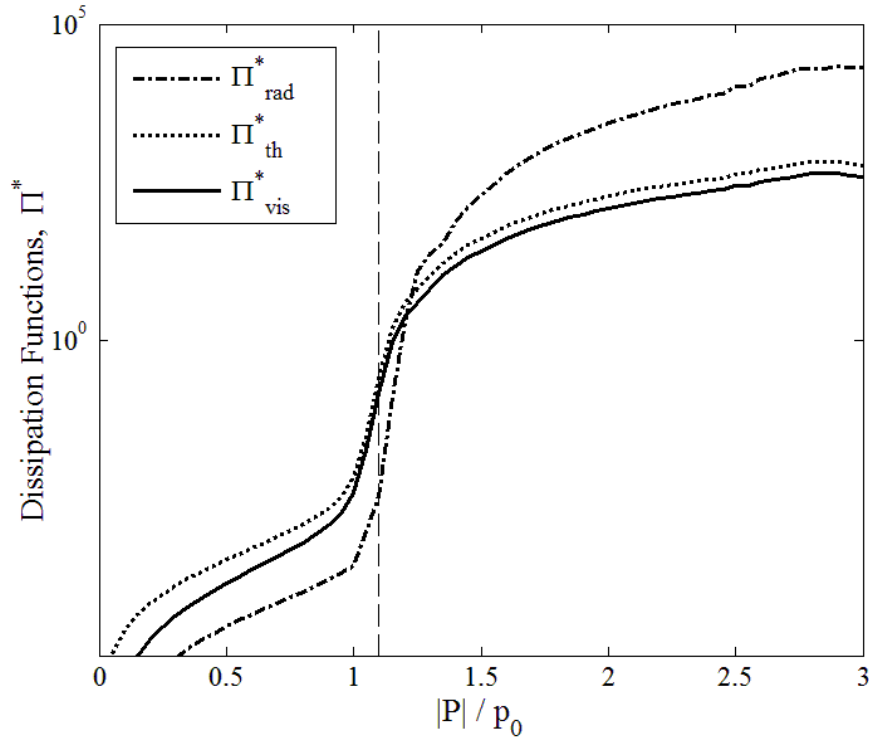


Figure 1: Thermal, viscous and acoustic dissipation for a $R_0 = 5\mu\text{m}$ bubbles in water. The thick solid line is the non-dimensional viscous dissipation; whereas thick dashed line represents the non-dimensional thermal dissipation and the dash-dot line the non-dimensional acoustic dissipation. Note that the non-dimensionalization is done with respect to $p_0 V_0 \omega$, i.e. $\Pi_v^* = \Pi_v / p_0 V_0 \omega$. The thin vertical dashed line represents the Blake threshold.

The dissipation functions are shown similarly for a $10\mu\text{m}$ bubble in Figure 2. Similar behavior can be observed when the evolution of dissipation vs. driving pressure is considered. For instance, the acoustic dissipation is the most dominant mechanism above the Blake threshold, whereas thermal losses are more effective below threshold. Comparison of two figures reveals that the amount of total dissipation under same conditions is less for bubbles with larger radius; which is in agreement with the results in Ref. [17].

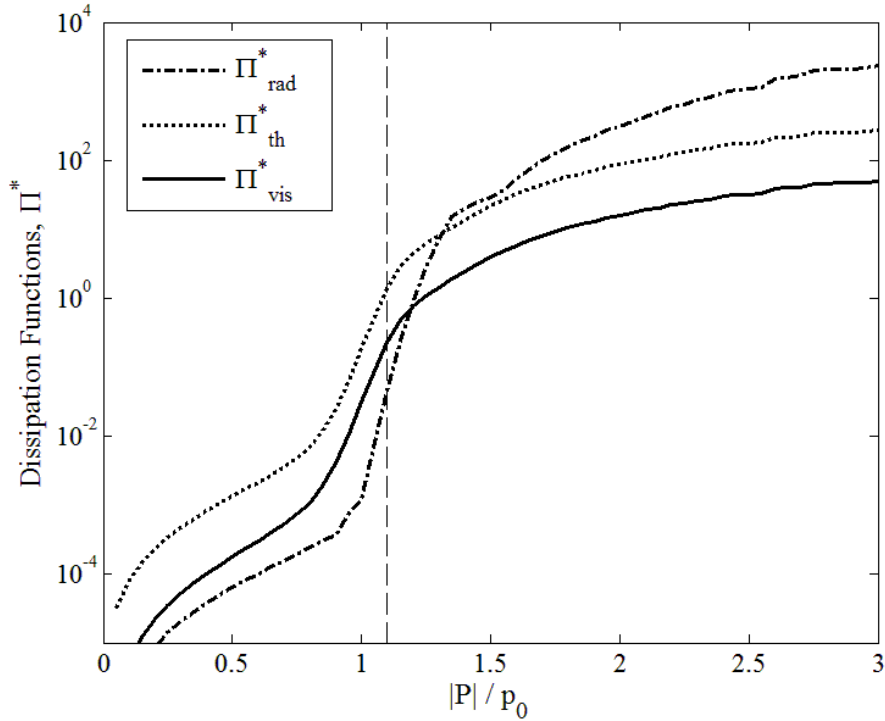


Figure 2: Thermal, viscous and acoustic dissipation for a $R_0 = 10 \mu\text{m}$ bubble in water. The line types are identical to the ones in Fig. 1.

The Helmholtz equation for the nonlinear wave propagation can be established starting from the Caflisch model [17]. The major difference of the model in comparison with the linear formulation is the dependence of the wavenumber on the spatial distribution of the sound pressure. The method assumes the decomposition of the pressure field into its harmonics and yields:

$$\nabla^2 P + k^2(|P|)P = 0. \quad (11)$$

where P is the amplitude of the first harmonic component of the oscillating pressure field. The equation for the real part of the wavenumbers reads:

$$\text{Re}(k^2) = \frac{\omega^2}{c^2} + \frac{4\pi R_0 \omega^2 N}{\omega_0^2 - \omega^2}. \quad (12)$$

It is further deduced that the imaginary part of the wavenumber (with the added corrections arising from compressibility effects) satisfies

$$\text{Im}(k^2) = -2\rho\omega N \frac{\Pi_{th} + \Pi_v + \Pi_{rad}}{|P|^2}. \quad (13)$$

In Fig. 3, the real and imaginary part of the wavenumber for the driving frequency 20 kHz, bubble volume fraction $\beta=0.005\%$ and the distribution of bubbles with uniform radius $R_0=5\ \mu\text{m}$, is plotted. The imaginary part of the wave number increases rapidly for driving amplitudes over the Blake threshold and it can be as high as the real part for very large driving amplitudes.

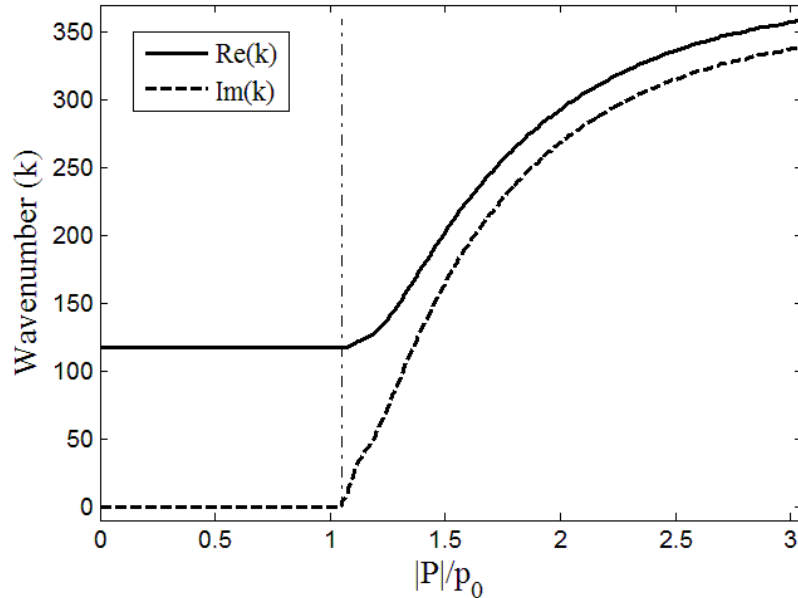


Figure 3: The real and imaginary part of the wavenumber used in the nonlinear wave propagation, evaluated by using Π_{th} , Π_{rad} and Π_v with $R_0 = 5\ \mu\text{m}$ and $\beta = 0.005\%$. Eqs. (12-13) are used to compute the values. Note that $\text{Re}(k^2)$ and $\text{Im}(k^2)$ should be first cast into a complex number, then square root of k^2 leads to the results presented in this figure.

3. Numerical method

The local boundary integral equation (LBIE) method for the solution of the Helmholtz equation was introduced in Ref. [32]. In the LBIE, source nodes are distributed inside the solution domain and a circular sub-domain is generated around each node. Next, one integral equation for the potential, arising from the application of Green's identities, is written at each source node. The 'companion solution' approach [33] is applied in order to eliminate the integral containing the gradient of the potential. The method encounters boundary integrals and domain integrals for the source nodes distributed over the global solution domain. These integrals can be evaluated by applying Gaussian integration procedure [34]. The unknown values for the potential at these Gaussian integration points are interpolated by using radial basis functions (RBFs).

In the case of wave propagation in bubbly liquids, the wavenumber is not constant throughout the domain and therefore the use of Helmholtz fundamental solution is not applicable. Hence, a formulation based on the Laplace fundamental solution should be applied.

3.1. The Local Boundary Integral Equation Method

Let us consider the following Helmholtz equation in a global solution domain Ω enclosed by the boundary $\Gamma = \partial\Omega$:

$$(\nabla^2 + k^2(P)) P(r) = 0, \quad (14)$$

where P is the pressure field and r is an arbitrary position vector inside the domain Ω . Eq. (14) should then be satisfied on any local sub-domain Ω_s . Applying the Green integral formula over a local sub-domain, Eq. (14) can be transformed into the following integral form:

$$P(r) + \int_{\partial\Omega_s} \frac{\partial p^*(r, \xi)}{\partial n} P(\xi) d\xi + \int_{\Omega_s} k^2(\zeta) p^*(r, \zeta) P(\zeta) d\zeta = 0 \quad (15)$$

where $\partial\Omega_s$ is the boundary of the local sub-domain. The modified fundamental solution p^* for a 2D Laplace equation is given by

$$p^*(R_\Omega) = -\frac{1}{2\pi} \ln(R_\Omega) + \frac{1}{2\pi} \ln(R_{\Omega_s}).$$

where R_{Ω_s} is the radius of the sub-domain (Fig. 4). Note that the first integral term in (15) is a surface integral over the boundary of the sub-domain and the second integral is a volume integral. The variable R_Ω is defined as the distance from the source point to the integration point, therefore corresponds to $R_\Omega = |r - \xi|$ and $R_\Omega = |r - \zeta|$ for the surface integral and the domain integral, respectively. The reason for using the modified fundamental solution in LBIE is the elimination of the terms related to the normal derivative by using the companion solution approach [32, 33].

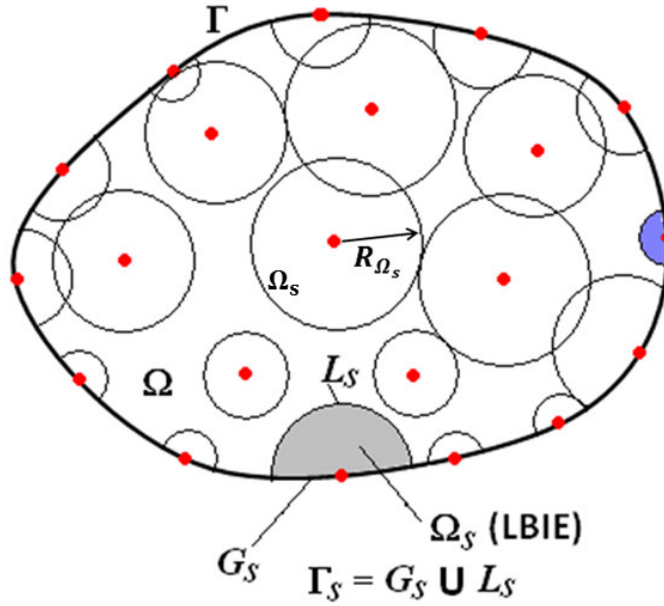


Figure 4: A sketch for the source nodes and local sub-domains placed in the solution domain Ω , and on the global boundary Γ .

For a given distribution of wavenumber k , the only unknown in Eq. (15) is P . $P(r)$ is the pressure at the centre of the local sub-domain, $P(\xi)$ in the first integral term is the pressure at any point on the boundary of the local sub-domain and $P(\zeta)$ in the second integral term is the pressure inside the local sub-domain. Note that $P(r)$ is a real variable which appears in the final matrix system, whereas $P(\xi)$ and $P(\zeta)$ are fictitious variables which are interpolated from the values of pressures in the neighbouring source nodes. Likewise, $k^2(\zeta)$ is interpolated throughout the local sub-domain from its known values at source nodes. The interpolation is performed using radial basis functions (RBF), the details of which are explained below.

If Dirichlet BCs are imposed on the part of the boundary where a source node is placed, the following equation would be applied:

$$P(r) = P_0. \quad (16)$$

If Neuman BCs are given on the part of the global boundary where r is located, the integral containing the gradient of the potential has to be evaluated, as it does not vanish on the global boundary [33, 35]. The following equation is applied:

$$\frac{1}{2}P(r) + \int_{L_s} \frac{\partial p^*(r, \xi)}{\partial n} P(\xi) d\xi - \int_{\Omega_s} k^2(\zeta) p^*(r, \zeta) P(\zeta) d\zeta = \int_{G_s} p^*(r, \zeta) \frac{\partial P(\zeta)}{\partial n} d\zeta \quad (17)$$

where L_s and G_s are the part of the boundary of the local sub-domain, inside the global domain and part of the global domain intersected by the local sub-domain, respectively (see Fig. 4). Note that L_s is not a full circle anymore, and that $d\zeta$ in the integral on the right hand side corresponds to infinitesimal integral element on the global boundary. The term on the right hand side of Eq. (17) can be called the acoustic source term. With all the terms of the integral kernel on the right hand side being known, the integration for that part of the equation gives a scalar value.

As discussed earlier, two types of integration are encountered for the local sub-domains, i.e. domain integration and boundary integration. Both types of integration are performed by

applying Gaussian integration procedure. When the integration is performed over the local sub-domain boundary, the Gaussian integration can be applied over the polar angle and as for the domain integrals it must be performed over both the radial direction and the angular direction [34]. At each of these Gaussian integration points, the values of the potentials (pressure in the present case) must be known. The unknown pressure value at each integration point is approximated by using radial basis functions (RBFs). The second order augmented thin plate spline $f(R) = R^4 \ln R$ is used throughout this work. In order to ensure the stability of the approximation, the frequency dependent polynomial terms are inserted into the basis [36, 37, 38]. Further details of the procedure for the RBF interpolation and the stability of the approximations can be found in [39, 40].

3.2. Nonlinear solution procedures

In this section, the nonlinear solution procedure is elaborated. Several error measurement criteria are used in the method; the definitions of which are given below:

The Root-mean-square error for P is defined as

$$e_{\text{RMS}} = \sqrt{\frac{\sum_{i=1}^{N_T} (P_i - P_i^{\text{ref}})^2}{N_T}} \quad (18)$$

where P_i is the potential at node i evaluated by the numerical scheme and P_i^{ref} is the ‘reference solution’ at node i .

The relative error at node i is defined as

$$e_{\text{Rel}}^i = \frac{|P_i - P_i^{\text{ref}}|}{P_i^{\text{ref}}} \times 100 \% \quad (19)$$

Note that the term ‘reference solution’ in the above equations will depend on the problem solved. If the analytical solution of the problem is known, then P_i^{ref} will refer to analytical solution at node i . If an analytical solution to a given problem is not available, the term ‘reference solution’ then may refer to the solution obtained by another numerical method or commercial software. Further, if a nonlinear solution procedure is required, the term reference solution may refer to solution in the previous step. How the RMS error and relative error measures are applied to the present problem are shown in Table 1.

For the solution of nonlinear wave propagation in a bubbly liquid, it is first essential to know the bubble volume fraction and bubble size distribution in the mixture. We assume that all bubbles in the mixture have the same radius. Initially, the Keller-Miksis equation (4) for the radial dynamics of bubbles is solved for a given bubble radius, a given driving frequency of the sound field, and for a range of sound pressure. Upon solution of (4), the thermal, Π_{th} , acoustic, Π_{rad} , and viscous, Π_v , dissipation per bubble are evaluated. Multiplication of Π_{th} , Π_{rad} and Π_v by the number of bubbles present in the mixture, N , yields the imaginary part of the wavenumber (given by equation (13)) as a function of driving pressure. The real part of the wavenumber is given by (12).

The nonlinear solution procedure is based on an iterative approach which takes the pressure dependent wavenumber as reference, e.g. the one given in Fig. 3. The first step of the algorithm is to solve for the Helmholtz equation in the bubble-free liquid for which the wavenumber is a constant (independent of pressure). With the obtained pressure distribution (non-dimensional values of $|p|$), the spatial distribution of the wavenumber at each source point is updated by using Fig. 3. The second iteration uses this updated wavenumber profile at each location. However, the result of the second solution is, in general, abrupt and unphysical because of the drastic change to the wavenumber and the corresponding high amount of damping introduced. In fact, completely damped wave profiles may be obtained with all values below Blake’s threshold. The overall solution thus oscillates in-between the two solutions, with and without bubbles present. Therefore, an approach which uses gradual increments in the wavenumber distribution should be employed.

The transition from a bubble-free to bubbly liquid is done using a ramp function centred at Blake's threshold, P_B . The value of the ramp function below P_B is a constant and the slope m of the ramp function above P_B increases at each iteration step of the solution process (see Fig. 5). The use of the ramp function essentially provides a smooth change in the spatial distribution of the wavenumber. Note that the slopes of the ramp functions for the real and imaginary parts of the wavenumber would not be identical since the real and imaginary values below and above P_B are different. However, they are iterated concurrently to reach their corresponding final values, while using the same iteration number.

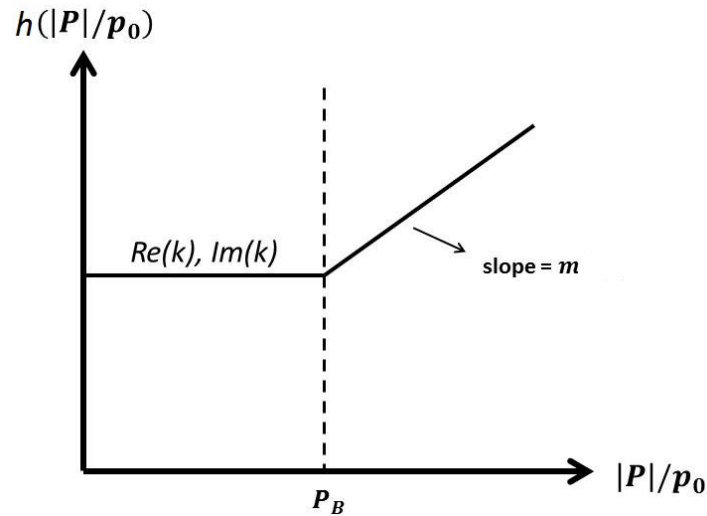


Figure 5: The ramp function used for updating the real and imaginary parts of the wavenumber from their initial value to their final profile given in Fig. 3. The supplementary file Video 1 shows how the wavenumber profile changes as the increments to the bubble void fraction are applied (see [web-link-1](#)).

A flow chart for the nonlinear solution procedure is given in Table 1. In order to ensure gradual increments, the number of total steps (N_s) to reach the final solution is set such that a discrete loop is constructed, i.e. $s = 0, 1, 2, \dots, N_s$ where s is the iteration number. Subsequently, the wavenumber k_i^s at a source node i , at the iteration step s is calculated by a simple interpolation procedure: The real part of k_i^s is given as

$$Re(k_i^s) = Re(k_0) + (s/N_s) \left(Re(k_i^f) - Re(k_0) \right) \quad (20)$$

and the imaginary part is given as

$$Im(k_i^s) = Im(k_0) + (s/N_s) \left(Im(k_i^f) - Im(k_0) \right) \quad (21)$$

In Eqns. (20)-(21), k_0 is the wavenumber in the pure liquid (the imaginary part of which is zero) and k_i^f is the wavenumber at the source node i obtained essentially from Fig. 3 for a given pressure value.

We may interpret the above process as if the bubble population gradually develops in the medium, though this is only a physical intuition. The value of N_s can be chosen arbitrarily provided that the increments are sufficiently small. N_s does not necessarily correspond to a certain amount of bubbles.

The main body of the method given in Table 1 consists of two nested loops. The outer *for* loop runs over the discrete index s , whereas the inner *do while* loop runs over the index j in which the total number of iterations is N_I , i.e. $j=1, 2, \dots, N_I$. The *do while* loop enforces the convergence to an acceptable solution $|P|^s$; each of these solutions can be referred to as $|P|_j^s$. The convergence of the *j-loop* at each step s is checked with an *if* statement by computing the RMS error of the solution at the j^{th} iteration with respect to solution at the $(j-1)^{\text{th}}$ iteration. This is given in the lines 15-19 of the flow chart in Table 1. Note that the total number of inner iterations N_I within the *j-loop* is *a priori* unknown. However, as it will be exemplified in the results section, N_I tends to increase significantly towards the later stages of the solution, i.e. when s tends to approach N_s .

Next, the *stability* issue should be addressed. The later stages of the solution are more cumbersome, one of the reasons being the increase in the k_i^s . Typically, given a value of s , drastic jumps with the pressure wave profile $|P|_j^s$ are observed which may last a few hundred inner iterations N_I without obtaining a RMS error within the specified tolerance value. In order

to avoid such unstable behaviour of the solution, an under-relaxation procedure is applied which is shown in lines 6-7 in Table 1. According to this, the relative error with respect to the previous iteration step is measured at each source node. If the maximum relative error within the solution domain exceeds the prescribed tolerance value, the under-relaxation is applied as in line 7. In the computations in this work, a maximum relative error of 3% within intermediate steps of the solution is allowed.

Finally, the oscillations of the solution should be addressed. Despite the applied stability and under-relaxation procedures, the nonlinear solution may suffer from oscillations at some stages. That is, given a value of s , the solution returns to one of the states within the iterations of the j -loop and repeats the same set of solutions $|P|_j^s$, which would cause N_l to tend to infinity if not controlled. This can be avoided by keeping the record of the previously obtained RMS errors within a j -loop and checking whether the RMS error obtained at the current j^{th} iteration is equal to any of the previously obtained $(j-1)$ RMS errors. This is illustrated within the lines 9-14 of the flow chart. In such case, the solution proceeds to the step $s+1$ as indicated in line 12.

Table 1: Flow chart for the nonlinear solution procedure

1	set the assembly
2	for ($s = 0: 1: N_s$)
3	do while ($e_{RMS,j} > \text{tolerance}$)
4	solve for the system
5	normalize the pressure ($P^* = P _j/p_0$)
6	find percentage relative error e_{Rel}^i for P^* (loop over all source nodes $i = 1: N_T$)
	restrict the solution from high oscillations (loop over all source nodes $i = 1: N_T$)
7	if $\max(e_{Rel}^i) > \%3$
	apply under-relaxation procedure $P_{j+1}^* = (1 - \alpha)P_j^* + \alpha P_{j+1}^*$
	end if
8	find RMS error for j^{th} iteration, i.e. $e_{RMS,j}$
9	check the repetitiveness of the solution by comparison to previous inner iterations, i.e.
10	do $k = 1 : j - 1$
11	if $e_{RMS,k} = e_{RMS,j}$
12	go to 16
13	end if
14	end do
15	if $e_{RMS,j} < \text{tolerance}$ ($1e - 6$) then
16	write the solution
17	set the inner solution (j -loop) RMS errors to zero
18	go to 21
19	end if
20	evaluate the wavenumber ($k^j = k(s, P_j^*)$)
	end do
21	increase the iteration number ($s = s + 1$)
22	set previous solution to the new solution ($P_s^* = P_{s+1}^*$)
23	evaluate the wavenumber ($k^{s+1} = k(s + 1, P_{s+1}^*)$)
24	end for

4. Applications of the method in bubbly liquids

In this section, we present the results of the simulations for the wave propagation in example sonoreactors. Two different examples are solved: In Section 4.1, a tube filled with bubbly water is considered. A moving piston on the left end of the tube supplies the acoustic forcing. A homogeneous distribution with constant bubble radius is employed for the bubble population field. Both linear and nonlinear wave propagations are solved; comparative results are given in order to demonstrate the corresponding attenuation of the waves. In Section 4.2, a sonoreactor design suggested by CEDRAT TECHNOLOGIES S.A., a participant in the SONO project, is examined. The acoustic propagation in a 2D cross-section of the actual sonoreactor is analysed and both the linear and the nonlinear wave propagations are solved. The effect of varying bubble size on the wave propagation is presented using a Gaussian type of distribution with minimum radius 10 μm and maximum radius 100 μm for the linear problem. In all examples, air bubble – water mixture is considered.

When interpreting the results, the distance between subsequent pressure nodes (or antinodes) gives insight about the wavelength, λ . Further, a drop in the pressure amplitude indicates an attenuation of the sound wave, since attenuation of the sound wave is conventionally quantified with the expression $\log(P_1/P_2)(x_1-x_2)$ where x_1 and x_2 are arbitrary locations and P_1 and P_2 are the pressure amplitudes at these locations respectively.

The built-in Fortran functions *getri* and the direct solver *pardiso* were used to compute the inverse matrix formed in the RBF interpolation and to solve the overall sparse system, where the system matrix elements are complex numbers. The models with 16,000 source nodes have been solved for 1D problem domain in Section 4.1 with uniform node distribution. In Section 4.2, LBIE method with 179,000 source nodes has been used. All the computations have been performed on an Intel Xeon 3.2 GHz workstation. For the 1D problem with 16,000 nodes, the solution required 150,000 iterations which took approximately 36 hours. For the 2D example with 180,000 nodes, the simulations took approximately 5.5 days.

4.1 Acoustic cavitation in 1D

The solution of linear and nonlinear wave propagation in a tube of length $L=0.1$ m filled with water is considered. At the left end of the tube, a piston with harmonic oscillations $U = U_0 \cos \omega t$ is considered where U_0 is the displacement amplitude and ω is the angular frequency of the driving sound field. The driving frequency is set at $f=20$ kHz. On the right end of the tube, an interface boundary is assumed and the acoustic pressure is set to zero. This particular setup allows to investigate the standing wave profiles in liquid filled tube. Note that this problem is identical to the one solved in [17].

4.1.1 Linear wave propagation

The wavenumber in the mixture as given by the linear theory (Eqs. (5-6)) is dependent on the driving frequency of the sound field (ω), ambient pressure in the liquid (p_0), surface tension (σ), liquid viscosity (μ), liquid density (ρ), velocity of sound in liquid (c) and distribution of the bubbles ($g(R)$). As a constant bubble size is assumed in this example, number of bubbles N can be found from Eq. (3) for a given value of the bubble volume fraction.

In Fig. 6, the results for the linear pressure propagation are shown for a mixture containing bubbles with $5 \mu\text{m}$ radius. The excitation value on the piston boundary is set as $U_0 = 5 \mu\text{m}$. The bubble volume fraction, β , is increased from 0.005 % to 0.012 %. Two distinct conclusions can be drawn: (i) the wavelength, therefore the phase velocity, in the mixture decreases with increasing bubble volume fraction, and (ii) the dissipation due to the bubbles and the total attenuation of waves in the medium gets larger, as can be seen from the reduced pressure wave amplitudes.

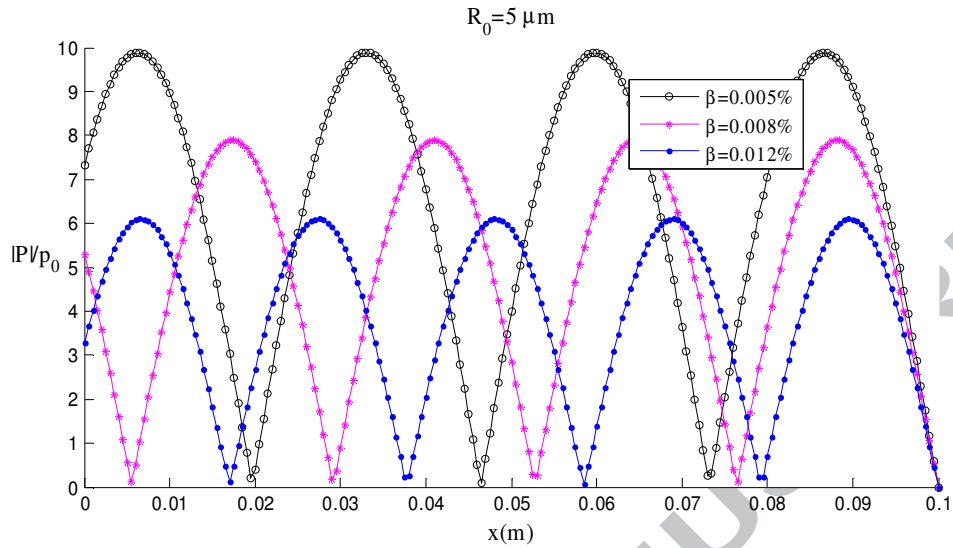


Figure 6: Pressure profiles with increasing bubble volume fraction, β . $U_0 = 5 \mu\text{m}$ and $R_0 = 5 \mu\text{m}$.

Note that the locations of the pressure antinodes, which are the indicative of cavitation zones, shift significantly along the tube as the bubble volume fraction changes, which is perhaps physically unrealistic (this will be better illustrated with comparisons to the nonlinear simulation results). Further, the linear propagation may be questioned in terms of the quantitative results obtained. Fig. 6 shows the amplitudes of the peak acoustic pressure as 6-10 bars for the bubble volume fractions used, which are quite high compared to commonly measured amplitudes at 20 kHz (typically 1.5-3 bar [17]).

4.1.2 Nonlinear wave propagation

In this section, the results from the nonlinear wave propagation model are presented. The governing equations are given through (11)-(13) along with the numerical solution procedure in Section 3.2. The bubble radius and the bubble volume fraction are kept constant at $R_0 = 5 \mu\text{m}$ and $\beta=0.005 \%$, respectively. For these values, the thermal, viscous and acoustic dissipation were given in Fig. 1 and the corresponding wavenumber profile as a function of driving pressure was shown in Fig. 3.

Figure 7 shows the acoustic pressure profiles for various excitation values of the source such as $U_0 = 0.2 \mu\text{m}$, $U_0 = 0.5 \mu\text{m}$ and $U_0 = 5 \mu\text{m}$. The lowest excitation case corresponds to a wave profile where the maximum pressure amplitude is below the Blake threshold. For this case, cavitation is not expected to occur and the standing wave profile is recovered. For the medium excitation case, the wave profile is damped at the pressure antinodes and further the dissipation by bubbles yields a nonzero acoustic pressure at the pressure nodes. For the highest excitation, the wave is drastically attenuated near the emitter. For the rest of the tube, the profile is similar to that of a standing wave, where the peaks occur at similar locations for the $U_0 = 0.2 \mu\text{m}$ and $U_0 = 0.5 \mu\text{m}$ cases. The rapid attenuation of the pressure waves near the emitter indicates high energy dissipation by cavitation bubbles. The results presented in Fig. 7 are very similar to the ones presented in Fig. 5 in Ref. [17], which were computed using COMSOL Multiphysics software.

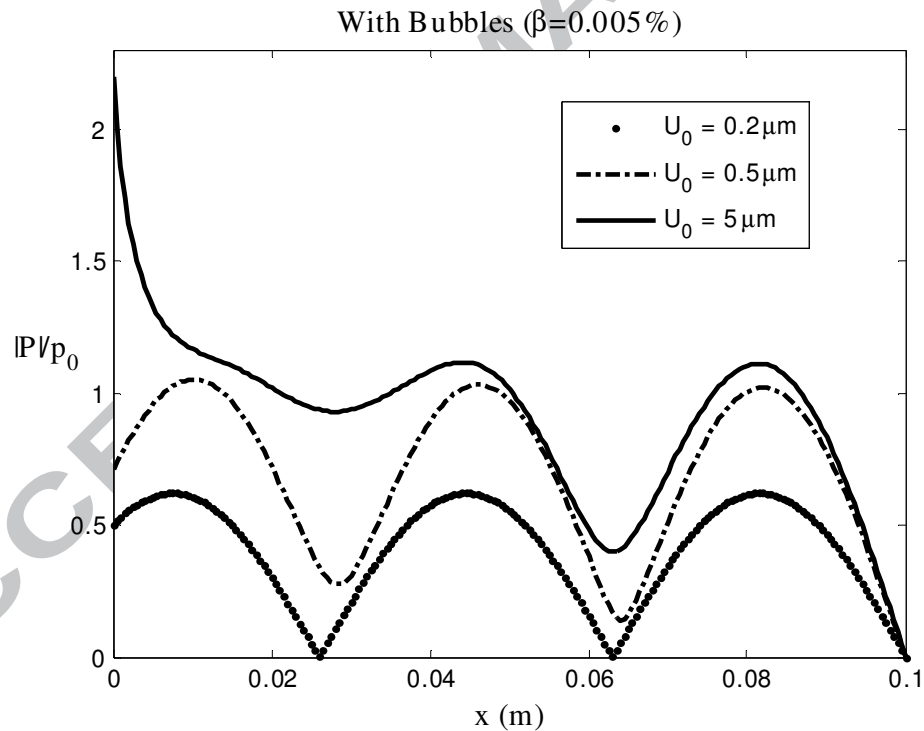


Figure 7: Pressure profiles for the cases: $U_0 = 0.2 \mu\text{m}$, $U_0 = 0.5 \mu\text{m}$ and $U_0 = 5 \mu\text{m}$. The attached Video 2 shows the convergence of the solution for the case $U_0 = 5 \mu\text{m}$, together with the text files which report the RMS error statistics (see [web-link-1](#)).

In Fig. 8, a comparison of the pressure profile in the pure liquid and those obtained from the linear and the nonlinear models is shown. The results demonstrate the substantial differences predicted in terms of the maximum amplitudes, as well as the close agreement of the nonlinear model (1-2 bar) with the measured realistic values as mentioned above.

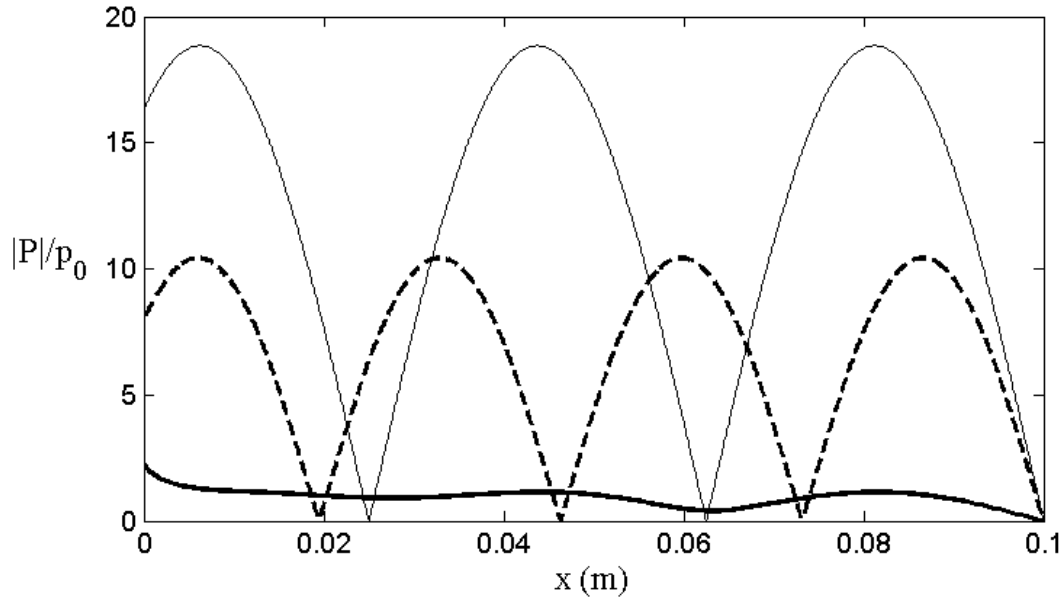


Figure 8: Comparison of wave profiles for a displacement amplitude of the acoustic source of $5 \mu\text{m}$. The thick line shows the nonlinear propagation, the dashed curve corresponds to the linear result and the thin line represents the pure liquid case.

For the nonlinear computations, the wavenumber is increased to its final value in $N_s = 1200$ steps. In addition, a maximum of 3% change is permitted for the relative error, over which an under-relaxation is applied for the whole pressure profile. As described in Table 1, a number of inner iterations are permitted for each increment of the wavenumber profile. For the later stages of the overall solution, the number of inner iterations increases significantly. Therefore, it has been set to a maximum of 400. The algorithm proceeds to the next iteration when the solution does not converge within the prescribed 400 iterations. For the under-relaxation parameter, $\alpha=0.2$ and $\alpha=0.3$ have been tried as separate computations; both of which converged. A tolerance

value 10^{-6} is employed for the RMS error. The overall solution requires approximately 150,000 iterations.

4.2 2D acoustic wave propagation in a model reactor

The 2D acoustic wave propagation in a model sonoreactor is examined. A sketch of the reactor is given in Figure 9. The reactor has three transducers and two heaters, all of which are of cylindrical shape. The transducer and heater locations in the x - y plane are marked as ‘T’ and ‘H’, respectively (see Fig. 9a). The textile fabric rolls over cylindrical cages, which are mounted at a distance of few centimeters from the transducers. The transducers produce both longitudinal and transversal vibrations; the motion of the transducer surface which is transverse into x - y plane may be conveniently assumed as radially symmetric because of the cylindrical geometry of the transducers. The heaters are used to maintain the mixture temperature at around 60°C . The reactor has eight inlets and an outlet for the recirculation of liquid. A perspective view sketch of the sonoreactor is given in Fig. 9a, and the x - y plane cross-section is given in Fig. 9b. The analysis of the wave propagation in the x - y plane is performed and the solution in the y - z plane and in the x - z is not considered. The transducer frequency is 20 kHz.

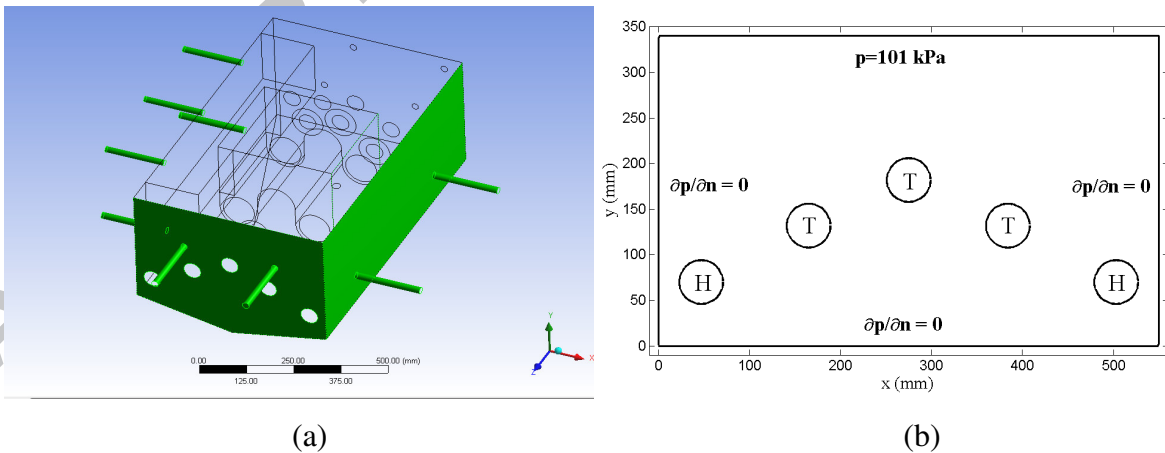


Figure 9: A sketch of the sonoreactor designed by CEDRAT Technologies. (a) perspective view (T – transducer, H – heater) and (b) x - y plane.

The following boundary conditions are applied on the surfaces of the sonochemical reactor model:

$$P|_{y=340 \text{ mm}} = 101 \text{ kPa}$$

$$\frac{\partial P}{\partial n}|_{x=0, x=550 \text{ mm}} = 0$$

$$\frac{\partial P}{\partial n}|_{y=0} = 0$$

The boundary conditions on the transducer surfaces were applied as follows:

$$\frac{\partial P}{\partial n}|_{\text{TS}} = -i\omega\rho\vec{v} \quad (22)$$

in which the velocity vector is determined by

$$\vec{v} = i\omega A e^{-i\omega t}, \quad (23)$$

where A is the maximum displacement on the transducer surface. A is chosen to be $0.5 \mu\text{m}$ during the simulations in the x - y plane. The normal derivative of the acoustic pressure on the surfaces of the heaters is given by

$$\frac{\partial P}{\partial n}|_{\text{H}} = 0. \quad (24)$$

Note that for the above mentioned geometry and the applied boundary conditions, the wave propagation in the x - y plane is symmetric with respect to the line $x=275$ mm.

4.2.1 Linear wave propagation

In this section, the linear wave propagation results are presented; in particular, the effects of bubble size distribution are investigated. In Fig. 10, the pressure profiles are displayed for a 10-100 μm bubble population with Gaussian distribution in order to observe the effect of increasing bubble volume fraction. The first sub-plot refers to the pure liquid case (where there are no bubbles), the maximum pressure for which reads approximately $28 p_0$ (~ 3 MPa) where p_0 is the atmospheric pressure. The pressure amplitude can be as low as $1-3 p_0$ when the bubbles are present. Clearly, the wavelength decreases with increasing β . Similarly to the previous 1D case, the attenuation gets larger when β increases. As it was the case in the previous example, the cavitation zones do not show a consistent pattern and resemble quite arbitrary behaviour with respect to the changes in the bubble volume fraction.

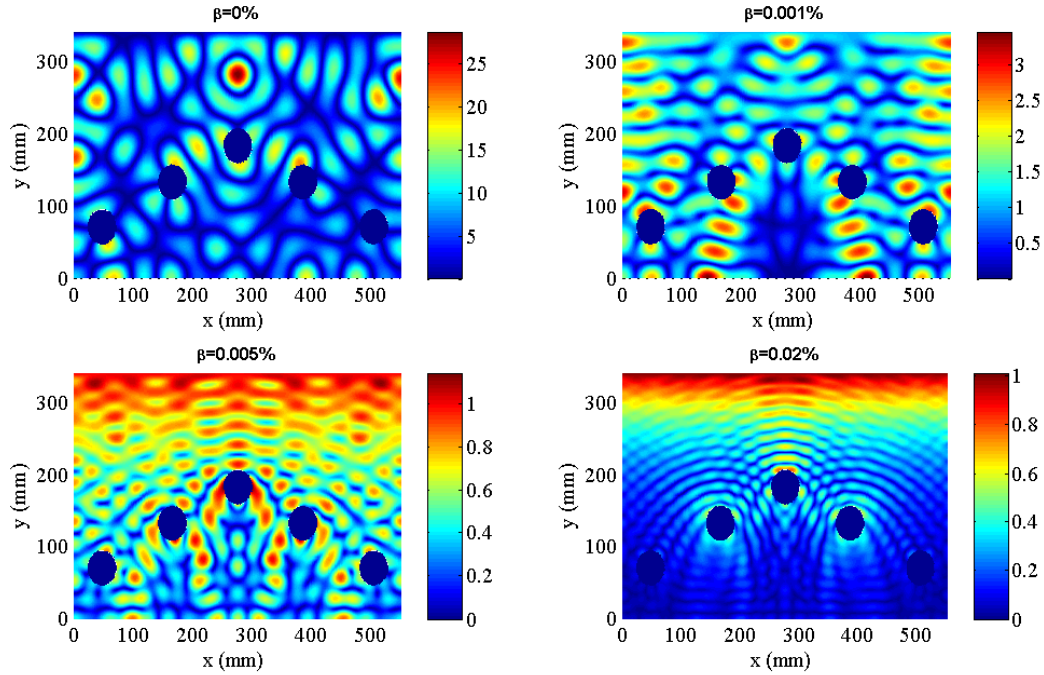


Figure 10: Effect of bubble volume fraction on the linear wave propagation ($R=10-100 \mu\text{m}$).

4.2.2 Nonlinear wave propagation

In this section, the results of the nonlinear wave propagation through the 2D cross-section of the actual sonoreactor are presented. For this case, a uniform bubble size distribution with $R_0 = 5 \mu\text{m}$ and $\beta=0.005 \%$, similar to Section 4.1.2, is adopted. The parameter values for under-relaxation α , total number of outer iterations (N_s) and inner iterations, the tolerance in RMS error and the maximum relative change in pressure amplitude are kept the same as in 1D nonlinear simulation. The extension of the present model to a range of bubble sizes requires the production of a set of results similar to those in Figs. 1 and 2, i.e. creating a discrete bubble radii array. However, their summation over the bubble radii range would result in a similar wavenumber profile to that given Fig. 3; therefore no significantly different results are expected.

In Figure 11, the linear vs. nonlinear propagation results are compared. In Fig 11a and 11b, the results of the initial stages of the nonlinear solution are displayed providing information on how the numerical solution evolves. The results are shown for very small values of s/N_s which

correspond to the first few iterations of the outer loop of the solution (see line 2 of Table 1). For instance, as the final solution is reached after 1200 increments in the outer loop, the plots shown in Fig. 11a and 11b correspond to the results obtained after 6 and 12 increments, respectively. Recall that the maximum pressure amplitude in liquid without bubbles is approximately $26 p_0$ as shown in the previous section. The wave amplitude decreases rapidly during the first few iterations of the solution, i.e. down to $15-12 p_0$ for the s/N_s values considered. Fig. 11c shows the final result of the nonlinear propagation modes, which is approximately $1.6 p_0$. The estimated maximum pressure amplitude in the linear theory (Fig. 11d) is approximately 4 times larger than its nonlinear counterpart. This shows that the attenuation is significantly underestimated in the linear theory.

Another major difference between the two approaches is the spatial distribution of the pressure wave peaks, hence the estimated cavitation zones. The nonlinear propagation indicates high energy cavitation zones in the immediate vicinity of the transducer surfaces – a fact also observed in experimental studies such as ultrasonic horns or other setups. Note that the linear theory does not predict such cavitation at or near the emitter surface in majority of the examples shown.

The general trend in the nonlinear solution starting from the initial stages is that a high amplitude pressure zone is pronounced at the emitter surface even for very low bubble volume fractions; the energy stored in the liquid in these areas then dissipates drastically, whilst keeping the similar qualitative behaviour. This is not the case for linear wave propagation results. In the linear case, the wavelength and the locations of pressure peaks (antinodes) or nodes are highly sensitive to the infinitesimal changes with the bubble void fraction and the bubble radius distribution as evident from the numerical results. Supplementary video and text files demonstrating the initial evolution and the convergence of the nonlinear solution can be found under [web-link-2](#). Three different video files are presented. Video 3 shows the full stages of the simulation at each increment to N_s (without inner iterations), Video 4 displays the results at each step of the outer loop with a smaller frame rate (first 11 increments of N_s) and Video 5 includes the inner iterations as well as the outer ones for the first 140 iterations.

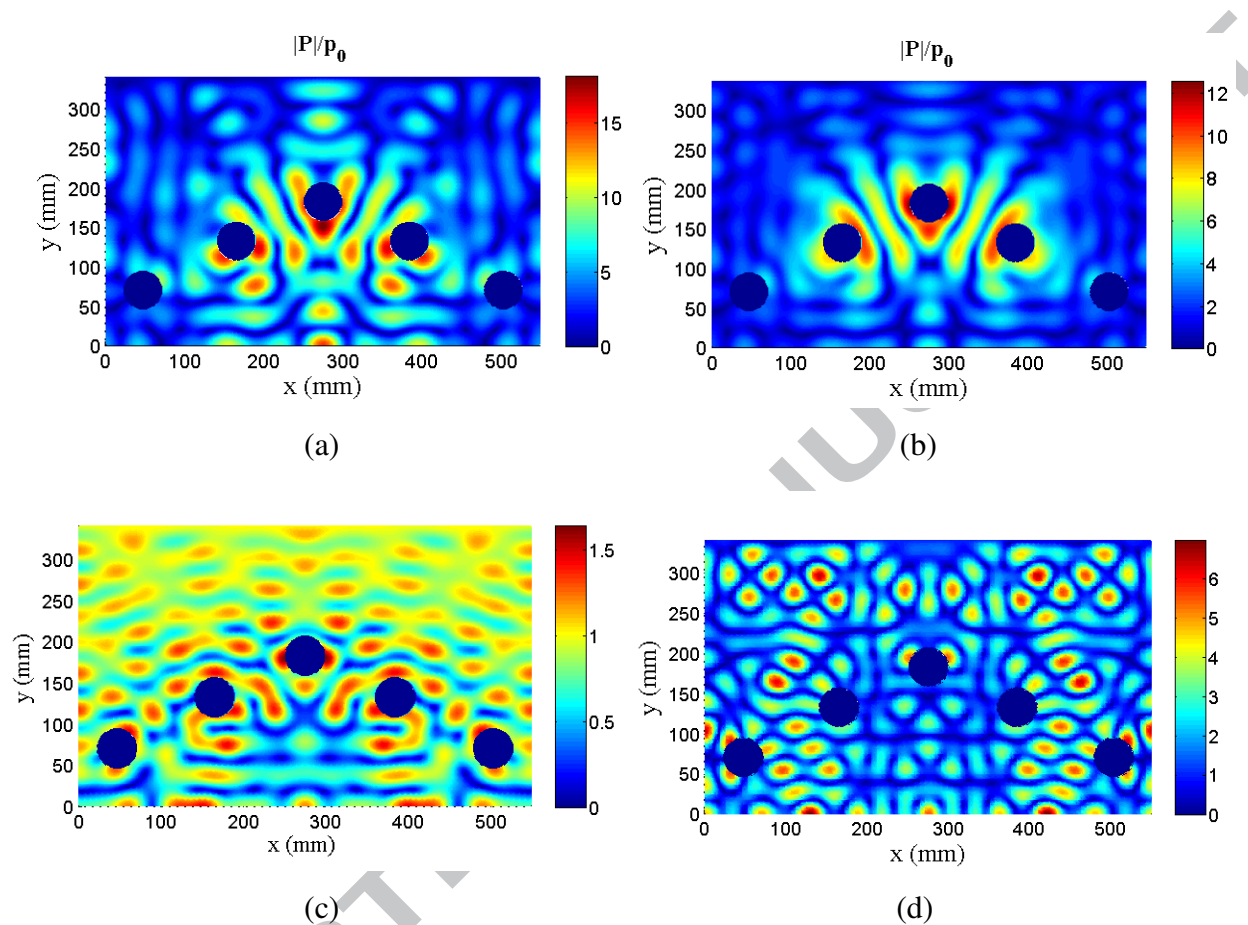


Figure 11: Pressure wave distribution obtained from the nonlinear model at (a) $s/N_s = 0.005$, (b) $s/N_s = 0.01$ and (c) $s/N_s = 1$ (final result) vs. (d) the linear model.

The example of the pilot plant sonoreactor shows significant difference in the predictions of the pressure distribution when using the linear and non-linear model. Whether the cavitation zone is required throughout the reactor or just in certain volumes, the linear model would not be capable of producing accurate predictions of the actual acoustic pressure. The non-linear model on the other hand could be used to obtain the required size and geometry of the reactor together with the design, required number and position of the transducers in order to achieve the desired intensity and location of cavitation zones.

The main difficulties when applying the non-linear model are related to the required input parameters for the preparation of the model and the computational requirements when solving the model. Among the input parameters we mention the bubble size distribution as well as the bubble volume fraction. These need to be either already known from previous experiments or from previous studies reported in the literature or they would need to be determined, which may not be straightforward [41, 42]. The CPU requirements could be significant for a full scale reactor especially if a three-dimensional model is used. The difficulties in achieving the convergence of the model may grow with the complexity and the size of the model. This is why the research in this area should continue as the authors see the non-linear model the adequate tool for designing and predicting the performance of sonochemical reactors in the future.

5. Conclusions

Acoustic wave propagation inside a sonochemical reactor is investigated by implementing both the linear and the nonlinear approaches. A numerical solution procedure is developed for the nonlinear case and verified by comparison to a previous example solved using the COMSOL Multiphysics software [17].

The existing linear theory provides some fundamental insights for the problem: the increase in the bubble volume fraction yields decreasing phase velocity and stronger damping (attenuation) of acoustic waves. However, the predictions of the location of the cavitation zones and the associated pressure amplitudes are not accurate. On the other hand, the nonlinear approach predicts correctly the location of the cavitation zones near the transducer surface, a feature commonly observed in practical applications. The linear theory appears to be overly sensitive to changes in bubble population field. In fact, small changes in the bubble size or bubble volume fraction results in significantly different pressure distribution even in a simple 1D configuration (see for example Figs. 6 and 10). The nonlinear method relies on a more robust representation owing to the nature of the wavenumber profile, hence produces consistent results. Although the nonlinear simulations have not been performed for larger bubble radii and volume fraction due to computational time requirements, it is anticipated that similar results would be

obtained in terms of pressure distribution in the medium, due to the behaviour of the wavenumber profile used in the nonlinear method.

The results suggest that though the linear model is straightforward for implementation and application, the non-linear model offers more realistic results and opportunity to predict the performance of the sonochemical reactor with higher accuracy, which leads to more optimal designs. The drawback of the non-linear models is the input parameters requirements, which might not be straightforward to obtain, and the CPU requirements for solving the model, especially if a 3D model is required.

Some remarks for future work are given as follows. The proposed numerical method is applicable to more complete models which would incorporate the multi-component gas dynamics inside the bubble, evaporation and condensation at the interface, chemical kinetics, etc. [43, 44]. The prerequisite for this is to define the relevant dissipation mechanisms and functions in a nonlinear fashion. Another necessary development is the incorporation of bubble nucleation, growth and formation of filamentary structures and streamers, as in [45, 46, 47], into the simulations which require the evaluation of Bjerkness forces exerted on bubbles. Further, the zero flux boundary condition at the surfaces of the heaters and the sonoreactor include some basic assumptions. A comprehensive way to account for more realistic boundary conditions is the coupling of elastic deformation and the wave propagation as implemented successfully in [48, 49, 50]. Finally, other numerical methods, such as, the finite element method (FEM), the boundary element method (BEM) or the finite volume method (FVM), may be employed to solve the Helmholtz equation in order to compare their convergence rates with the current numerical approach.

Acknowledgements

The findings in this paper were obtained as part of the SONO project, contract number: 228730, European Commission – Seventh Framework Programme (FP7-NMP-2008-Large-2). The authors are grateful to Olivier Louisnard for the helpful discussions. The first author H. Dogan is currently funded by National Environment Research Council UK (Grant number

NE/J022403/1, Principal Investigator Prof T.G. Leighton). Part of this research was completed at the Wessex Institute of Technology, where the authors worked previously.

References

- [1] W. D. Song, M. H. Hong, B. Lukyanchuk and T. C. Chong, "Laser-induced cavitation bubbles for cleaning of solid surfaces," *J. Appl. Phys.*, vol. 95, no. 6, p. 2952–2956, 2004.
- [2] P. R. Gogate and A. M. Kabadi, "A review of applications of cavitation in biochemical engineering/biotechnology," *Biochemical Engineering Journal*, vol. 44, pp. 60-72, 2009.
- [3] K. Gotoh, K. Harayama and K. Handa, "Combination effect of ultrasound and shake as a mechanical action for textile cleaning," *Ultrason. Sonochem.*, vol. 22, pp. 412-421, 2015.
- [4] T. G. Leighton and R. O. Cleveland, "Lithotripsy," *Proceedings of the Institution of Mechanical Engineers, Part H: Journal of Engineering in Medicine*, vol. 224, no. 2, pp. 317-342, 2010.
- [5] P. R. Gogate, "Cavitation reactors for process intensification of chemical processing applications: A critical review," *Chemical Engineering and Processing: Process Intensification*, vol. 47, no. 4, pp. 515-527, 2008.
- [6] T. J. Mason, "Developments in ultrasound - Non-medical," *Progress in Biophysics and Molecular Biology*, vol. 93, no. 1-3, pp. 166-175, 2007.
- [7] F. J. Keil and K. M. Swamy, "Reactors for sonochemical engineering - Present status," *Reviews in Chemical Engineering*, vol. 15, no. 2, pp. 85-155, 1999.

- [8] Z. Fu and V. Popov, "Parametric study of acoustically-driven microbubble cavitations in a sonochemical reactor," *Ultrasonics Sonochemistry*, vol. 21, no. 1, pp. 415-427, 2014.
- [9] V. S. Sutkar, P. R. Gogate and L. Csoka, "Theoretical prediction of cavitation activity distribution in sonochemical reactors," *Chemical Engineering Journal*, vol. 158, no. 2, pp. 290-295, 2010.
- [10] P. R. Gogate and A. B. Pandit, "Sonochemical reactors: scale up aspects," *Ultrasonics Sonochemistry*, vol. 11, pp. 105-117, 2004.
- [11] P. R. Gogate, V. S. Sutkar and A. B. Pandit, "Sonochemical reactors: Important design and scale up considerations with a special emphasis on heterogeneous systems," *Chemical Engineering Journal*, vol. 166, no. 3, pp. 1066-1082, 2011.
- [12] V. S. Sutkar and P. R. Gogate, "Design aspects of sonochemical reactors: techniques for understanding cavitation activity distribution and effect of operating parameters," *Chem. Eng. J.*, vol. 155, pp. 26-36, 2009.
- [13] K. Suslick and G. J. Price, "Applications of ultrasound to material chemistry," *Annu. Rev. Mater. Sci.*, vol. 29, pp. 295-326, 1999.
- [14] N. Perkas, G. Amirian, G. Dubinsky, S. Gazit and A. Gedanken, "Ultrasound assisted coating of nylon 6,6 with silver nanoparticles and its antibacterial activity," *Journal of Applied Polymer Science*, vol. 104, pp. 1423-1430, 2007.
- [15] I. Perelshtein, G. Applerot, N. Perkas, G. Guibert, S. Mikhailov and A. Gedanken, "Sonochemical coating of silver nanoparticles on textile fabrics (nylon, polyester and

- cotton) and their antibacterial activity,” *Nanotechnology*, vol. 19, no. 24, p. 245705, 2008.
- [16] O. V. Abramov, A. Gedanken, Y. Koltypin, N. Perkas, I. Perelshtein, E. Joyce and T. J. Mason, “Pilot scale sonochemical coating of nanoparticles onto textiles to produce biocidal fabrics,” *Surface & Coatings Technology*, vol. 204, pp. 718-722, 2009.
- [17] O. Louisnard, “A simple model of ultrasound propagation in a cavitating liquid. Part I: Theory, nonlinear attenuation and traveling wave generation,” *Ultrasonics Sonochemistry*, vol. 19, no. 1, pp. 56-65, 2012.
- [18] R. E. Caflisch, M. J. Miksis, G. C. Papanicolaou and L. Ting, “Effective equations for wave propagation in a bubbly liquid,” *J. Fluid Mech.*, vol. 153, pp. 259-273, 1985.
- [19] O. Louisnard, “A simple model of propagation in a cavitating liquid. Part II: Primary Bjerkness force and bubble structures,” *Ultrason. Sonochem.*, vol. 19, pp. 66-76, 2012.
- [20] C. Vanhille and C.-F. Pozuelo, “Nonlinear Ultrasonic Propagation In Bubbly Liquids : A Numerical Model.,” *Ultrasound in Med. And Biol.*, vol. 34, no. 5, pp. 792-808, 2008.
- [21] C. Vanhille and C. Campus-Pozuelo, “Numerical simulations of three-dimensional nonlinear acoustic waves,” *Ultrason. Sonochem.*, vol. 20, pp. 963-969, 2013.
- [22] G. Servant, J.-P. Caltagirone, A. Gerard, J.-L. Laborde and A. Hita, “Numerical simulation of cavitation bubble dynamics induced by ultrasound waves in a high frequency reactor,” *Ultrason. Sonochem.*, vol. 7, pp. 217-227, 2000.
- [23] G. Servant, J.-L. Laborde, A. Hita, J.-P. Caltagirone and A. Gerard, “Spatio-temporal dynamics of cavitation bubble clouds in a low frequency reactor : comparison between

- theoretical and experimental results,” *Ultrasonics Sonochemistry*, vol. 8, pp. 163-174, 2001.
- [24] G. Servant, J.-L. Laborde, A. Hita, J.-P. Caltagirone and A. Gerard, “On the interaction between ultrasound waves and bubble clouds in mono- and dual-frequency sonoreactors,” *Ultrason. Sonochem.*, vol. 10, pp. 347-355, 2003.
- [25] S. Dahnke and F. J. Keil, “Modelling of Linear Pressure Fields in Sonochemical Reactors Considering an Inhomogeneous Density Distribution of Cavitation Bubbles.,” *Chem. Eng. Sci.*, vol. 54, pp. 2865-2872, 1999.
- [26] S. Dahnke, K. M. Swamy and F. J. Keil, “Modelling of Three-Dimensional Linear Pressure Fields in Sonochemical Reactors with an Inhomogeneous Density Distributions of Cavitation Bubbles : Comparison of theoretical and experimental results,” *Ultrasonics Sonochemistry*, vol. 6, pp. 31-41, 1999.
- [27] Y. A. Kobelev and L. A. Ostrovskii, “Nonlinear acoustic phenomena due to bubble drift in a gas-liquid mixture,” *J. Acoust. Soc. Am.*, vol. 85, no. 2, pp. 621-629, 1989.
- [28] K. W. Commander and A. Prosperetti, “Linear pressure waves in bubbly liquids: Comparison between theory and experiment,” *J. Acoust. Soc. Am.*, vol. 85, pp. 732-746, 1989.
- [29] I. Tudela, V. Saez, M. D. Esclapez, M. I. Diez-Garcia, P. Bonete and J. Gonzalez-Garcia, “Simulation of the spatial distribution of the acoustic pressure in sonochemical reactors with numerical methods: A review,” *Ultrasonics Sonochemistry*, vol. 2014, pp. 909-919, 2014.
- [30] A. Prosperetti, L. Crum and K. Commander, “Nonlinear bubble dynamics,” *J. Acoust. Soc.*

Am., vol. 83, pp. 502-514, 1988.

- [31] R. Jamshidi and G. Brenner, "Dissipation of ultrasonic wave propagation in bubbly liquids considering the effect of compressibility to the first order of acoustical Mach number," *Ultrasonics*, vol. 53, pp. 842-848, 2013.
- [32] H. Dogan, V. Popov and E. H. Ooi, "Dispersion analysis of the meshless local boundary integral equation and radial basis integral equation for the Helmholtz equation," *Engineering Analysis with Boundary Elements*, vol. 50, pp. 360-371, 2015.
- [33] T. Zhu, J. -D. Zhang and S. N. Atluri, "A local boundary integral equation (LBIE) method in computational mechanics, and a meshless discretization approach," *Computational Mechanics*, vol. 21, no. 3, pp. 223-235, 1988.
- [34] E. H. Ooi and V. Popov, "An efficient implementation of the radial basis integral equation method," *Engineering Analysis with Boundary Elements*, vol. 36, no. 5, pp. 716-726, 2012.
- [35] J. Sladek, V. Sladek and N. S. Atluri, "Application of the local boundary integral equation method to boundary-value problems," *International Applied Mechanics*, vol. 38, no. 9, pp. 1025-1047, 2002.
- [36] S. Suleau and P. Bouillard, "One-dimensional dispersion analysis for the element-free Galerkin method for the Helmholtz equation," *International Journal for Numerical Methods in Engineering*, vol. 47, no. 6, pp. 1169-1188, 2000.
- [37] S. Suleau, A. Deraemaeker and P. Bouillard, "Dispersion and pollution of meshless solutions for the Helmholtz equation," *Computer Methods in Applied Mechanics and*

- Engineering*. 2000; 190(5-7): 639-657., vol. 190, no. 5-7, pp. 639-657, 2000.
- [38] E. H. Ooi, V. Popov and H. Dogan, "Three dimensional solution for acoustic and transport problems using the radial basis integral equation method," *Applied Mathematics and Computation*, vol. 218, no. 18, pp. 9470-9488, 2012.
- [39] V. Popov and T. T. Bui, "A meshless solution to two-dimensional convection-diffusion problems," *Engineering Analysis with Boundary Elements*, vol. 34, pp. 680-689, 2010.
- [40] H. Dogan, V. Popov and E. H. Ooi, "The radial basis integral equation method for the solving the Helmholtz equation," *Engineering Analysis with Boundary Elements*, vol. 36, no. 6, pp. 934-943, 2012.
- [41] P. R. Gogate, S. Mujumdar and A. B. Pandit, "Large-scale sonochemical reactors for process intensification: design and experimental validation," *Journal of Chemical Technology and Biotechnology*, vol. 78, no. 6, pp. 685-693, 2003.
- [42] V. S. Sutkar and P. R. Gogate, "Mapping of cavitation activity in high frequency sonochemical reactor," *Chemical Engineering Journal*, vol. 158, no. 2, pp. 296-304, 2010.
- [43] G. Huake, D. Fuster and C. Dopazo, "Dynamics of a single cavitating and reacting bubble," *Physical Review E*, vol. 75, pp. 066310 (1-14), 2007.
- [44] B. D. Storey and A. J. Szeri, "A reduced model for cavitation physics for use in sonochemistry," *Proc. R. Soc. Lond. A*, vol. 457, pp. 1685-1700, 2001.
- [45] U. Parlitz, R. Mettin, S. Luther, I. Akhatov, M. Voss and W. Lauterborn, "Spatio-temporal Dynamics of Acoustic Cavitation Bubble Clouds," *Phil. Trans. R. Soc. Lond. A*, vol. 357,

pp. 313-334, 1999.

- [46] D. Krefting, R. Mettin and W. Lauterborn, "High speed observation of acoustic cavitation erosion in multibubble systems.," *Ultrasonics Sonochemistry*, vol. 11, pp. 119-123, 2004.
- [47] R. Mettin, S. Luther, C. -D. Ohl and W. Lauterborn, "Acoustic cavitation structures and simulations by a particle model," *Ultrason. Sonochem.* , vol. 6, pp. 25-29, 1999.
- [48] K. Yasui, T. Kozuka, T. Tuziuti, A. Towata, Y. Iida, J. King and P. Macey, "FEM calculation of an acoustic field in a sonochemical reactor," *Ultrason. Sonochem.* , vol. 14, pp. 605-614, 2007.
- [49] O. Louisnard, J. Gonzalez-Garcia, I. Tudela, J. Klima, V. Saez and Y. Vargas-Hernandez, "FEM simulation of a sono-reactor accounting for vibrations of the boundaries," *Ultrasonics Sonochemistry*, vol. 16, no. 2, p. 250–259, 2009.
- [50] I. Tudela, V. Sáez, M. D. Esclapez, P. Bonete, H. Harzali, F. Baillon, J. González-García and O. Louisnard, "Study of the influence of transducer-electrode and electrode-wall gaps on the acoustic field inside a sonoelectrochemical reactor by FEM simulations," *Chemical Engineering Journal*, vol. 171 , no. 1, pp. 81-91, 2011.

Web-references

1. <https://www.dropbox.com/sh/ifjl4k4yn24bisc/AACt34-Afau48Caj9PUYbGR7a?dl=0>
2. <https://www.dropbox.com/sh/eg11xxbuxxoul89/AAD-1pnGBHbXmL6dmqADABZ2a?dl=0>

Highlights

- Analysis of acoustic wave propagation in bubbly liquid in a sonoreactor was carried out
- Linear and nonlinear propagation models were compared
- Nonlinear models produce more realistic results of the intensity and location of cavitation zones
- The nonlinear model showed to be more suitable for the design of sonoreactors

ACCEPTED MANUSCRIPT